

MICROSTRUCTURE AND CORROSION PROPERTIES OF ADDITIVELY MANUFACTURED ALUMINIUM ALLOY AA2024

*O. Gharbi, D. Jiang, D.R. Feenstra, S. Kairy, Y. Wu, C.R. Hutchinson, and N. Birbilis

*Department of Materials Science and Engineering, Monash University, Victoria, Australia
(Corresponding author: oumaima.gharbi@monash.edu)*

ABSTRACT

Recent developments in metal-based additive manufacturing (AM) technology have generated considerable interest in multiple industries, owing to flexibility in design and the ability to produce final components in their net shape. The AM of high-strength aluminium alloys has not been widely explored, due to findings of undesirable microstructures leading to short fatigue life and poor fracture toughness; restricting the application of AM to lower strength aluminium alloys (with cast-like Al-alloy compositions) to date. Herein, aluminium alloy AA2024 (Al-3.6Cu-1.2Mg) was additively manufactured *via* selective laser melting (SLM), with the resultant microstructures and corrosion properties characterised and compared to wrought AA2024-T3. Microstructural characterisation was carried out using transmission electron microscopy (TEM), revealing SLM produced AA2024 included a population of θ -phase (Al₂Cu) in preference to S-phase (Al₂CuMg) typical of wrought AA2024. Additionally, the corrosion properties were investigated by potentiodynamic polarisation in a range of NaCl concentrations, whilst elemental corrosion rates were also determined (including for open circuit exposure conditions) and quantified *in situ* with an inductively coupled plasma mass spectrometer coupled with an electrochemical flow cell. Results revealed a significant improvement in the corrosion resistance, and elemental dissolution of AM prepared 2024 relative to wrought AA2024-T3.

KEYWORDS

Aluminium alloys, Additive manufacturing, Corrosion, AA2024

INTRODUCTION

Aluminium alloys remain the preferred candidate materials in applications requiring a balance of low density and strength. The ability to produce net shape components from aluminium alloys has accelerated due to recent developments in metal-based additive manufacturing (AM) technology, including selective laser melting (SLM) and powder bed 3D printing. The AM of Al-alloys, including Al-Si-Mg (namely AlSi10Mg), has become widespread commercially in recent years. Alloys including AlSi10Mg offer reliable and reproducible production by AM, however such alloys (and variants thereof) are not high strength alloys. The pursuit of higher strength AM Al-alloys presents significant merit to multiple industries; however, such higher strength AM Al-alloys have not been widely studied to date. The solidification of high strength Al-alloys during conventional (casting) operations needs to be executed in a manner that avoids so-called 'hot-tearing', which can arise as a result of the solute type and loading. A report on the solidification of a high strength Al-alloy prepared by AM, along with factors related to solidification, was recently covered by Pollock and co-workers (Martin et al., 2017). It was reported that AM of high-strength aluminium alloys (which have to date been principally based on the compositions of wrought high strength Al-alloys) may lead to undesirable microstructures that reduce fatigue life and result in poor fracture toughness; presently limiting the application of AM to lower strength aluminium alloys (with cast-like Al-alloy compositions) to date.

Recently, Zhang et al. successfully printed a dense and microcrack-free Al-Cu-Mg alloy via SLM (Zhang, Zhu, Qi, Hu, & Zeng, 2016). In that study, the alloy exhibited ultra-fine supersaturated dendrite structure, enabled by the rapid cooling process inherent to the SLM process. In addition, microhardness testing demonstrated improved microhardness and tensile strength as compared to the wrought AA2024 in the annealed state. Although the study of Zhang et al. demonstrated the presence of homogeneous elemental distribution throughout the alloy, fine and coarse grains were found. More recently, Caiazza et al. studied the prospect of using direct metal deposition to prepare AA2024 in the context of repairing components (Caiazza, Alfieri, Argenio, & Sergi, 2017). Although the authors successfully demonstrated cladding along the scanning direction, the coalescence of dispersoids and the presence of grain boundaries precipitates around the heat affected zones and in the fusion zones led to a notable softening in such areas. In the work herein, we report upon AA2024 as prepared by selective laser melting, which has to date not been widely reported upon.

In the context of properties that are critical to Al-alloys, corrosion performance is one important parameter. For high-strength Al-alloys that gain their desirable mechanical properties from the development of heterogeneous microstructures, corrosion is also influenced by such microstructural heterogeneity (Birbilis et al., 2016; Birbilis & Buchheit, 2005; Buchheit, 1997; Buchheit, Grant, Hlava, Mckenzie, & Zender, n.d.; Lebouil, Tardelli, Rocca, Volovitch, & Ogle, 2014; Nisancioglu, 1990; Scamans, Birbilis, & Buchheit, 2010; Scully, Knight, Buchheit, & Peebles, 1993). More specifically, high-strength Al-alloys tend to suffer from localised corrosion, arising from microgalvanic interactions between the alloy matrix and the 'type' of particles present. Particles in the broad sense refer to all of constituent particles, dispersoids, and precipitates (the latter responding to thermal treatment). Localised corrosion of Al-alloys is a widely studied topic, with the morphology and rate of corrosion highly dependent on the alloy particle population. In addition to electrochemical testing, the methods for studying localised corrosion of Al-alloys normally include electron microscopy, and more recently, scanning probe methods (Birbilis, Cavanaugh, & Buchheit, 2006; Buchheit & Birbilis, 2010; Buchheit et al., n.d.; Loïc Lacroix, Ressler, Blanc, & Mankowski, 2008; Leblanc & Frankel, 2002; Zhang & Frankel, 2002). Such techniques are useful in their own right, but are often qualitative, with no direct measurement of quantitative corrosion rate and no specific ability to unequivocally quantify elemental dissolution (even in the case of scanning electrochemical microscopy).

The ability to use online methods (such as an electrochemical flow cell coupled to a spectrometer) for direct assessment of elemental corrosion rates was demonstrated by Ogle and co-workers (Mokaddem, Volovitch, Rechou, Oltra, & Ogle, 2010; Ogle, 2012; Serdechnova, Volovitch, Brisset, & Ogle, 2013). The technique termed AESEC (atomic emission spectroelectrochemistry) allows for the study of corrosion rates

in real time, in open circuit or polarised conditions. The application of the AESEC method to the study of Al-alloy corrosion permits a significant step-change in the ability to quantify corrosion, in particular, answering questions such as ‘what elements are actually dissolving?’ and ‘at what rates are specific elements dissolving?’. Work by Gharbi et al. has demonstrated the ability of AESEC to truncate the study of Al-alloy corrosion in the context of various high-strength Al-alloys (Gharbi, Birbilis, & Ogle, 2016, 2017), when coupling AESEC with microstructural characterisation. Herein, the use of online ICP and the AESEC method were utilised in order to provide a quantification of the corrosion of AM prepared AA2024. In addition, the comparison between the elemental dissolution of AM prepared 2024 and wrought 2024-T3, the latter a widely studied Al-alloy, is presented herein.

EXPERIMENTAL

Materials

Commercial AA2024 powder supplied by LPW Technology with a spherical size varying between 20–63 μm was used to produce AM2024 *via* selective laser melting (SLM). Selective laser melting was carried out using a Concept Laser Mlab cusing R, and employing an argon purged atmosphere. The laser power was fixed at 80 W and the laser scan speed was varied between 60 to 540 mm/s. Layer thickness during the SLM process was 25 μm and the distance between laser passes (also termed the hatch distance) was 80 μm . Commercial AA2024-T3 sheet (2 mm thick) was used for comparison and the precise composition of all specimens tested are given in Table 1. The compositions were determined using Inductively Coupled Plasma Atomic Emission Spectroscopy (ICP-AES) at an accredited laboratory (Spectrometer Services, VIC. Australia).

Table 1. Composition (in wt. %) of alloys tested

Element	AA2024 Powder	AM2024	AA2024-T3
Al	Bal	Bal	Bal
Cu	3.84	3.6	4.2
Mg	1.27	1.17	1.4
Fe	0.11	0.11	0.11
Mn	0.36	0.36	0.5
Si	0.72	0.78	0.07
Zn	0.01	0.01	0.02
Ti	<0.01	0.01	0.02
Ni	<0.005	<0.005	0.006
Zr	<0.005	<0.005	0.014
Cr	<0.005	<0.005	0.005

Microstructural Analysis

Transmission electron microscopy (TEM) was performed on specimens prepared from AM2024. Specimens for TEM were prepared by the focussed ion beam (FIB) lift-out technique, carried out using an FEI[®] Quanta 3D FEG equipped with a Ga ion beam. An FEI[®] Tecnai G2 T20 and an FEI[®] Tecnai G2 F20 S-TWIN FEG TEM, both operated at 200 kV, were used for the imaging, electron diffraction and Energy-dispersive X-ray spectroscopy (EDXS). Prior to analysis, specimens were plasma cleaned in Ar and O₂ gas mixture for 2 min using a Gatan[®] Solarus 950 advanced plasma system. Scanning-TEM (STEM) images were collected in bright field (BF) and high angle annular dark field (HAADF) modes. Diffraction contrast and atomic number (Z)-contrast information were provided by BF and HAADF-STEM images, respectively. A Bruker X-flash X-ray detector was used to collect EDXS maps, and data analysis was performed using the Bruker Esprit 1.9 X-ray software.

Potentiodynamic Polarisation Testing

Alloy specimen were cold mounted using an epoxy, and mechanically ground under ethanol to a 2000 grit finish and ultrasonically cleaned prior each experiment. The sample (working electrode, WE) was

introduced in a Princeton Applied Research® K0235 flat cell containing a saturated calomel electrode (RE) and a platinum mesh counter electrode (CE).

Polarisation testing using a Bio-logic® VMP-3 potentiostat was conducted in NaCl at various concentrations (0.6, 0.1 and 0.01 M NaCl) at a scan rate of 1 mV s⁻¹ commencing from +20 mV (vs. OCP) to -1.8 V_{SCE} in the case of cathodic polarisation testing; and from -20 mV (vs. OCP) to -0.1 V_{SCE} in the case of anodic polarisation testing. Prior to polarisation testing, all samples were exposed to the electrolyte at OCP for 20 min in order to allow electrode stabilisation. All reagents used were reagent grade and the solutions were used 'as-mixed'.

ICP-MS and Electrochemical Cell Flow Coupling

The online analysis of corrosion rates, including the quantification of elemental dissolution, were performed using an inductively coupled plasma mass spectrometer (ICP-MS) coupled with a three-electrode electrochemical flow cell. In the testing, 0.01 M NaCl was carried through the flow cell at a constant flow rate (0.13 ± 0.02 mL min⁻¹) and injected to the ICP-MS in order to quantify dissolution rates in real time. The alloy dissolution rate (expressed in µg s⁻¹cm⁻²) can be calculated according to Equation 1:

$$v_M = C_M f / A \quad (1)$$

where C_M (in ppm) is the concentration of the released elements, f is the electrolyte flow rate, A is the exposed surface area (0.4 cm²). The dissolution rate can also be expressed according to Faraday's law as an equivalent current density, according to Equation 2:

$$i_M = z F v_M / M \quad (2)$$

where z the oxidation state of the dissolved ion, M is the molar mass and F = 96485 C mol⁻¹. Equation 2 permits the determination of i_M, the elemental current density in µA cm⁻². The flow cell employed has a single compartment, as the reference electrode (RE) is sealed from one side and the Pt counter electrode (CE) is positioned at the output and serves as a tube where the electrolyte flows to ICP-MS. A more detailed schematic can be found in (Hou et al., 2016). A Perkin Elmer NexION® 2000 ICP-MS was used in this work and the mass selected for the elements was ²⁷Al, ²⁴Mg, ⁶³Cu, ⁵⁷Fe, ⁵⁵Mn, and their detection limits (C_{2σ}), were 1.4 ppb for Al, 3.1 ppb for Cu and Mn, 2.6 ppb for Mg and 1.3 ppb for Fe, respectively. All the reagents used for these experiments were prepared with ultra-pure water (18 MΩ.cm Millipore™) and high purity NaCl (ACS reagent >99.9%) for ICP-MS analysis purposes.

RESULTS AND DISCUSSION

Microstructural Analysis of 3D Printed 2024

Images of AM2024 and the corresponding EDXS maps are presented in Figure 1, revealing the presence of multiple particles with a size ranging from 10 nm to 0.5 µm, for the case of optimised AM conditions which led to a high (84%) consolidation.

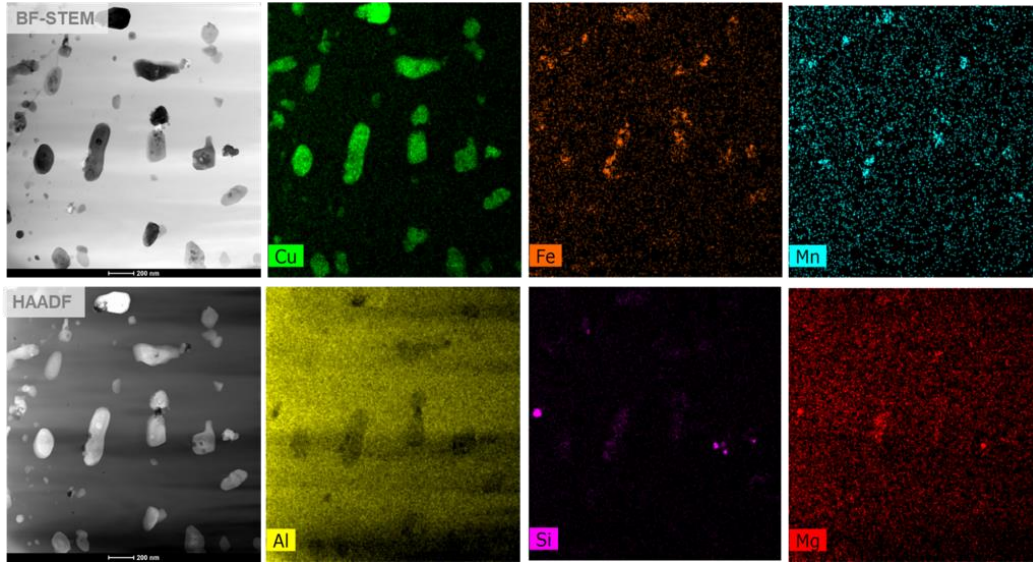


Figure 1. BF-STEM and HAADF-STEM images of AM2024, presented with the corresponding EDXS maps for Cu, Fe, Mn, Al, Si and Mg. The SLM conditions employed for the sample shown are laser power at 80 W, laser scan speed of 300 mm/s. The layer thickness was 25 μm and the distance between laser passes (also termed the hatch distance) was 80 μm

As revealed by the corresponding EDXS maps (in Figure 1), the majority of particles in AM2024 are Cu-rich, and more specifically were determined to be θ -phase (Al_2Cu). Structural and diffraction analysis is not reported here, however (not shown here), the prevalence of θ -phase in AM2024 was confirmed. This finding highlights the significant microstructural differences that can arise from AM production. In addition, other phases, such as Si-rich, Mg-rich, (Si-Mg)-rich and (Fe-Mn-Si)-rich particles were found to be occasionally clustered with θ -phase particles.

Although Mg is revealed in the EDXS maps (Figure 1), the result suggests that S-phase (Al_2CuMg) was not a significant ‘precipitate’ formed in AM2024; rendering a significant proportion of Mg present in solid solution. The term ‘precipitate’ is used in a colloquial sense herein, as strictly speaking, the microstructure of AM2024 is a microstructure evolved from ‘cooling’, as opposed to a microstructure formed from aging (with or without artificial heating) following solutionising, as is the case in AA2024-T3. The microstructures reported here for AM2024 are “as SLM produced”, with no subsequent heat treatment applied.

The clustering of the Si-rich, Mg-rich or (Fe-Mn-Si) and (Si-Mg)-rich particles with θ -phase particles can be, to some extent, representative of complex constituent-type particles as recently reported in a study by Birbilis et al. (Birbilis et al., 2016), and Hughes et al. (Boag et al., 2009), who have identified compositional variations throughout a single constituent particle in AA2024-T3. Such constituent particles displayed complex structures, with the presence of two, two-phase structure types; namely the Cu-rich variant depleted in Si and Mn, and the Cu-lean variant, enriched in Si and Mn. Analogously, two distinct types of particles can be observed amongst the Cu-rich particles found in AM2024; Mg-Si rich particles, and Fe-Mn-Si particles. In AM2024, the complex precipitates do not correspond to the precise constituent particles reported in wrought AA2024-T3 [7, 23], the genesis of constituent particles in AM prepared Al-alloys remains at this stage unclear (and a topic of future work).

Potentiodynamic Polarisation in 0.01, 0.1 and 0.6 M NaCl

Microstructural analysis of the AM2024 demonstrated the apparent non-existence of micrometre sized particles – which is suggestive that the localised corrosion of AM2024 may be unique to that of

wrought AA2024, which contains a significant population of micrometre sized particles. Consequently, it is of interest to investigate the electrochemical behaviour of AM2024, including the potentiodynamic polarisation response, including the study of anodic (i.e. dissolution) and cathodic (i.e. oxygen reduction) kinetics - which are nominally influenced by microstructural features in the alloy. To this end, separate anodic and cathodic potentiodynamic polarisation tests were conducted following a 20 min immersion (conditioning at OCP), with the results displayed in Figure 2.

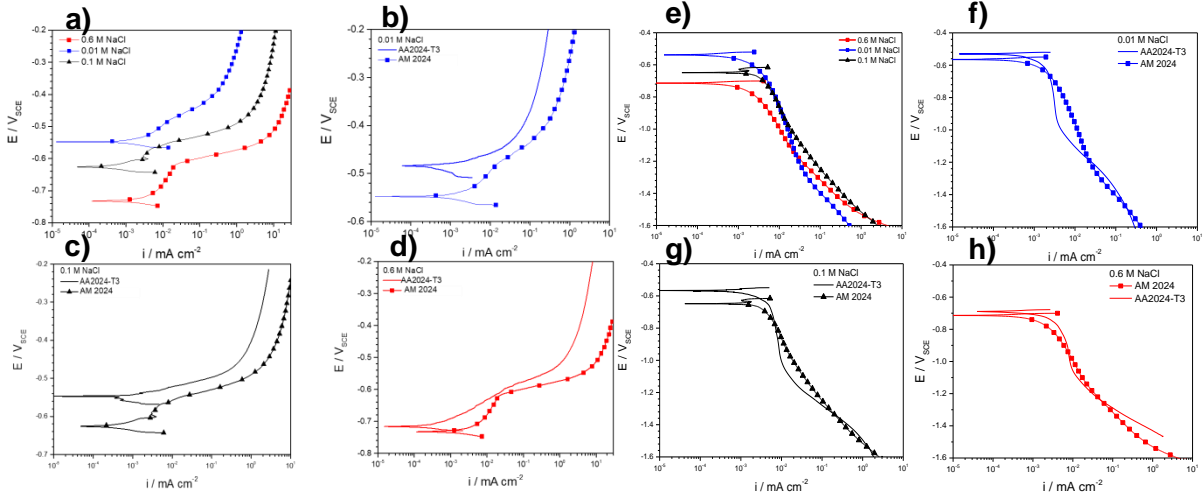


Figure 2. Anodic and cathodic polarisation test results from AM2024 and wrought AA2024-T3 in 0.01 M, 0.1 M and 0.6 M NaCl. Figure a) and e) correspond to anodic and cathodic polarisation of AM2024 in 0.01M,0.1M and 0.6M NaCl. The anodic polarisation data of AM2024 is compared to the AA2024-T3 in 0.01M (b)),0.1 M NaCl (c)), and 0.6 M NaCl (d)) and the cathodic branch is compared in e) (0.01M NaCl), g) (0.1M NaCl) and h) 0.6 M NaCl

The effect of chloride concentration on the AM2024 was clearly evident from visual inspection of anodic polarisation data; whereby the corrosion potential was shifted from $-0.52 V_{SCE}$ for 0.01 M NaCl to $-0.74 V_{SCE}$ for 0.6 M NaCl. This shift in corrosion potential corresponds to the ability of increasing chloride concentration to activate the anodic (dissolution) reaction. Concomitantly, the presence of a passive window was readily discernible for the three chloride concentrations, occurring at approximately $+90 mV$ vs. E_{corr} , allowing a clear distinction between E_{corr} and E_{pit} , where E_{pit} is the breakdown potential above which stable pitting can occur (Figure 1 a)). In the case of wrought AA2024-T3, anodic current increases rapidly, indicating pitting occurring at all potentials more positive than E_{corr} (including at E_{corr}) for all chloride concentrations tested. The improved pitting resistance in AM2024 can be principally explained by the absence of S-phase, on the basis of well documented studies relating to the discrete dissolution of S-phase in AA2024-T3. In fact, the pitting potential of S phase and θ -phase as function of chloride concentration has been documented in several studies whereby according to Birbilis and Buchheit, S-phase exhibits a corrosion potential varying from $-0.956 V_{SCE}$ in 0.01 M NaCl to $-0.695 V_{SCE}$ in 0.6 M NaCl. In the case of AA2024-T3, S-phase undergoes spontaneous selective dissolution (i.e. dealloying) at the potential tested, resulting in the absence of passive window. The dealloying of S-phase is concomitant with the selective dissolution of Mg (and Al), with the accumulation of Cu. Conversely, θ -phase has been reported to undergo little dissolution in aqueous chloride solutions, presenting a corrosion potential ranging from $-0.592 V_{SCE}$ for 0.01 M NaCl to $-1.061 V_{SCE}$ in 0.6 M NaCl (Birbilis & Buchheit, 2005). In the case of the AM2024 sample, the absence of S-phase can rationalise the notable shift in the pitting potential, as the possibility of any dealloying or localised dissolution at potentials in the vicinity of the E_{corr} is avoided.

No significant difference between the results of cathodic polarisation testing were observed between both alloys tested, as represented in Figure 1e, 1f, 1g and 1h. Furthermore, the rate of the cathodic reaction did not vary significantly for the three chloride concentrations tested.

The microstructural observations revealed a marked decrease of the average ‘particle’ size (where such particles represent a diverse population of what may be termed constituents, dispersoids and precipitates in wrought alloys), with the average particle size not exceeding 0.5 μm . This refinement of microstructural features would imply that a notable decrease of the local cathodic:anodic surface area ratio—in comparison to AA2024-T3 (where an average size of the constituent particles of approximately 1 to 30 μm is expected (Polmear, 1995)).

Dissolution Profiles of AA2024-T3 and AM2024 in 0.01M NaCl at OCP and Under Anodic Polarisation

The elemental dissolution rates of the AM2024 and wrought AA2024-T3 were monitored using the coupling of an electrochemical flow cell and an ICP-MS, a technique derived from the so-called AESEC method, with the results are illustrated in Figures 3a and 3b.

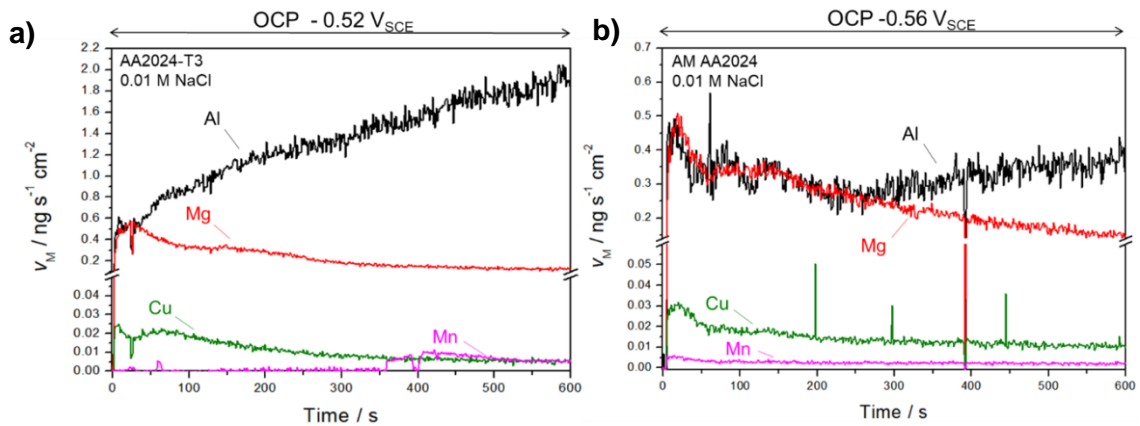


Figure 3. Dissolution profiles of Al, Cu, Mg, Mn as a function of time of a) AA2024-T3 and b) AM 2024 at open circuit potential in 0.01 M NaCl determined by the coupling of an electrochemical flow cell and an ICP-MS

The specimens tested were exposed at the OCP condition in 0.01M NaCl for a period of 10 min, and the results presented as a function of exposure time. The Al, Cu, Mg and Mn dissolution rates are expressed in $\text{ng s}^{-1}\text{cm}^{-2}$ (noting that the Fe signal was below the detection limit). The OCP was monitored for each experiment and the average value determined was $\sim -0.645 V_{\text{SCE}}$ for AA2024-T3 (Figure 3 a)). In the case AA2024-T3, when the electrolyte came into contact with the alloy, the dissolved Al signal increased to $v_{\text{Al}} \sim 0.45 \text{ ng s}^{-1}\text{cm}^{-2}$ during the first 50 s of electrolyte exposure, and continued to steadily rise to a maximum of $\sim 1.9 \text{ ng s}^{-1}\text{cm}^{-2}$ at the end of the experiment duration. Similarly, Mg and Cu dissolution rate increased rapidly at $t = 0$, reaching a value of $v_{\text{Mg}} \sim 0.45 \text{ ng s}^{-1}\text{cm}^{-2}$ and $v_{\text{Cu}} \sim 0.025 \text{ ng s}^{-1}\text{cm}^{-2}$, during the first 50 s exposure, and slowly decreasing to $0.01 \text{ ng s}^{-1}\text{cm}^{-2}$ and $0.15 \text{ ng s}^{-1}\text{cm}^{-2}$, respectively. Conversely, the Mn signal was not detected during the first 350 s of the experiment, after which the Mn signal rose to quickly reach a value of $0.015 \text{ ng s}^{-1}\text{cm}^{-2}$.

In the case of AM2024 exposed to 0.01 M NaCl for a period of 10 min, the response observed is reported in Figure 3b). When the electrolyte came into contact with the AM2024 sample at $t = 0$, the Al, Cu, Mg and Mn dissolution rates instantaneously increase. Interestingly, Al and Mg exhibit nearly identical dissolution profiles during the first 250 s of immersion (v_{Al} and $v_{\text{Mg}} \sim 0.27 \text{ ng s}^{-1}\text{cm}^{-2}$) and subsequently slowing to $\sim 0.15 \text{ ng s}^{-1}\text{cm}^{-2}$, whilst the dissolved Al signal subsequently remained relatively stable until the end of the experiment duration. The Mg dissolution rate indicated that: i) Mg dissolution mainly stems from the Al matrix and ii) the Mg dissolution rate is significantly higher than what would be expected for congruent (i.e. uniform) dissolution owing to the bulk alloy composition. Concomitantly, Cu and Mn dissolution commenced when the sample was exposed to the electrolyte, reaching dissolution rates of $v_{\text{Cu}} \sim 0.03 \text{ ng s}^{-1}\text{cm}^{-2}$ and $v_{\text{Mn}} \sim 0.05 \text{ ng s}^{-1}\text{cm}^{-2}$, whilst remaining relatively stable during the experiment

duration. Interestingly, the presence of Cu spikes at $t = 200, 300,$ and 450 s, are indicative of the detachment of Cu rich particles from the sample.

The dissolution profiles of the wrought AA2024-T3 and AM2024 exposed at OCP conditions reveal a significant decrease of Al corrosion rate for the AM2024 ($\sim 1.9 \text{ ng s}^{-1} \text{ cm}^{-2}$ vs $0.4 \text{ ng s}^{-1} \text{ cm}^{-2}$), as Al dissolution rate is reduced by 4.8. However, Cu and Mg exhibited identical dissolution profiles for both alloys, whilst Mn being an exception and not dissolving during the first ~ 350 s of the experiment for the case of the AA2024-T3. Such results (Figure 4) may also be expressed as ratios, whereby for each alloy the Cu, Mg and Mn dissolution profiles were divided by the respective corresponding Al signal. The dissolution ratios $v_{\text{Cu}}/v_{\text{Al}}$, $v_{\text{Mg}}/v_{\text{Al}}$ and $v_{\text{Mn}}/v_{\text{Al}}$ are used herein as means to assess the proportion of alloying element dissolving between the alloys.

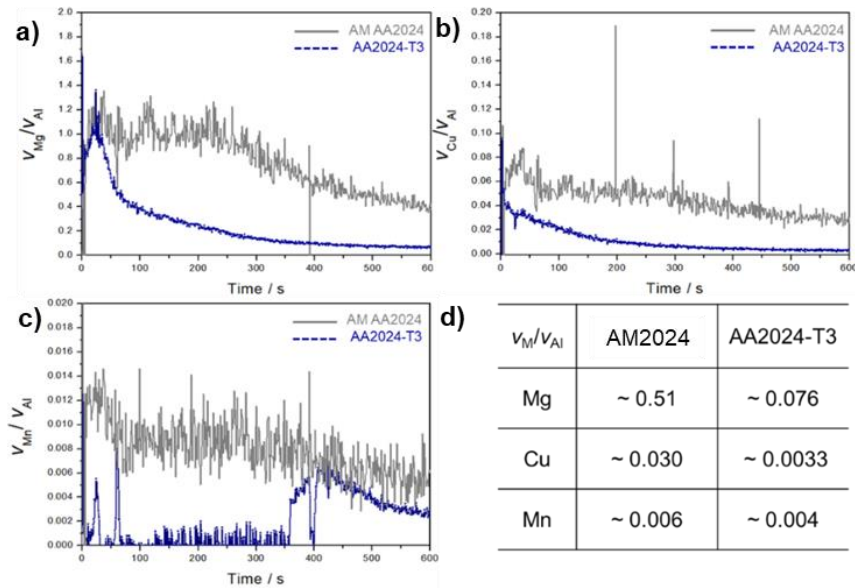


Figure 4. Comparison of Mg, Cu and Mn dissolution rate divided by their respective Al signal from AM2024 and AA2024-T3, and d) the determined average values. Results indicate that for Mg and Cu, the quantity of alloying elements dissolved is of one order magnitude higher for the AM2024

The OCP immersion experiments highlighted the difference in dissolution profiles of both alloys, as for the AM2024, the proportion of alloying elements dissolving (Mg and Cu) is around one order of magnitude higher than the wrought AA2024-T3. Aluminium dissolution commenced at the same rate at the beginning of the experiment ($0.4 \text{ ng s}^{-1} \text{ cm}^{-2}$), however, the Al dissolution profiles increased rapidly for AA2024-T3 reaching $2.0 \text{ ng s}^{-1} \text{ cm}^{-2}$, whereas the AM2024 remained stable. Such behaviour could be explained by i) the difference in alloy composition (locally) or ii) the microstructural features present in the respective alloys (i.e. particle type (and stoichiometry/chemistry), size and distribution) – owing to the SLM solidification process. The first hypothesis in this specific case cannot be readily realised, as the chemical analysis of the alloy reveals similar compositions (particularly Cu and Mg which are the main alloying element in the 2xxx series Al-alloys). On the other hand, the microstructural analysis demonstrated a substantial difference in the particle type, size and distribution. The TEM characterisation revealed the presence of sub-micron sized intermetallic particles, homogeneously distributed. Equally critical, the absence of S-phase precipitates within the AM2024 alloy. Whilst S-phase is a strengthening precipitate in AA2024-T3 (with nanoscale precipitates formed during natural aging), S-phase is also susceptible to dealloying, trenching and pitting. It is apparent however, that due to the local melting and subsequent rapid cooling in the SLM process, that S-phase formation and the clustering of Cu containing constituent particles are not kinetically favoured (and suppressed) yielding a refined microstructural feature

size with nano-sized Al-Cu-Fe-Mn impurities evenly distributed on the surface. Such nano-scale Cu-rich particles may be more readily detached from the alloy surface when matrix dissolution occurs.

To further characterise the effect of the microstructure on the elemental dissolution kinetics, simultaneous ICP-MS and anodic polarisation were carried out following the OCP measurement, shown in Figures 5a and 5b. The elemental dissolution currents i_{Al} , i_{Cu} , i_{Fe} and i_{Mg} were determined from the elemental dissolution rate using Faraday's law (assuming $n = 3$ for Al and Fe, and $n = 2$ for Cu and Mg) expressed as a function of time and electrochemical potential.

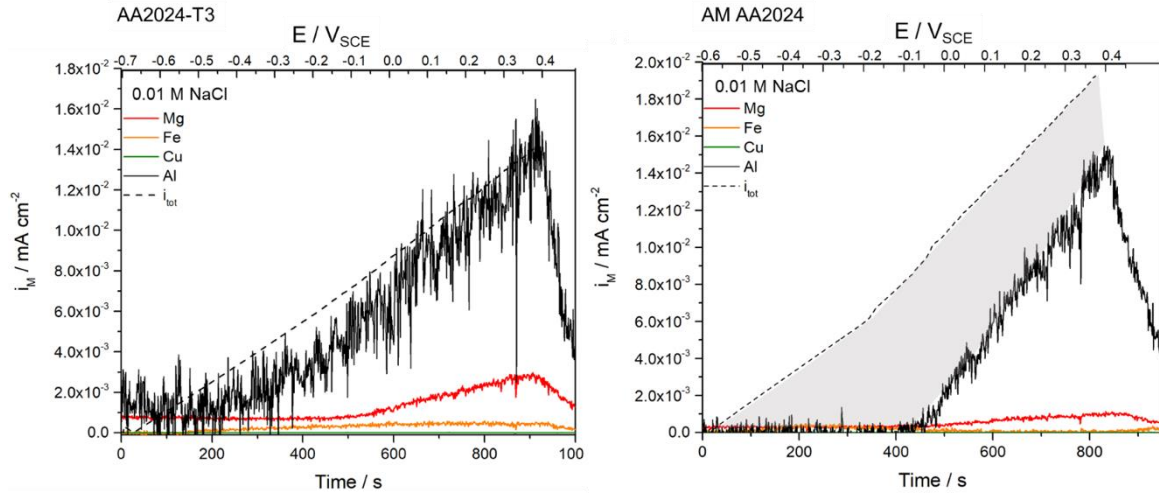


Figure 5. Elemental dissolution profiles Al, Cu, Mg and Fe (the Mn signal was below the detection limit, i.e. <3.1 ppb) during anodic polarisation testing. i_{tot} represents the total current signal collected from the potentiostat (and is represented by the dashed line). The left plot represents results obtained for AA2024-T3, whilst the right plot represents the results obtained for AM2024. The area shaded in grey illustrates the difference between i_{tot} and i_{Al} , attributed to Al-oxide film formation and growth

In the case of AA2024-T3, the Al dissolution current begins to rise linearly, closely following the total current i_{tot} , to a maximum value of 0.014 mA cm^{-2} at 0.4 V_{SCE} . These findings highlight a comparative Faradaic yield throughout, indicating that the majority of the oxidised species remain in solution and are carried to the ICP-MS via the flow cell. Simultaneously, the Mg dissolution rate remained constant ($\sim 0.001 \text{ mA cm}^{-2}$) and only rose after $\sim 550 \text{ s}$, which corresponded to $\sim -0.1 \text{ V}_{SCE}$, and increasing to each $i_{Mg} = 0.002 \text{ mA cm}^{-2}$. On the other hand, Fe dissolved steadily as the anodic potential was applied, reaching $0.6 \times 10^{-3} \text{ mA cm}^{-2}$.

The difference in the AESEC determined dissolution currents between AM2024 and wrought AA2024-T3 was immediately apparent, and clearly illustrated by the offset between the total current i_{tot} and i_{Al} as seen in Figure 5b. Such a scenario in the data is typically observed when insoluble species precipitate on the surface following their oxidation, hence forming a protective oxide on the surface. This phenomenon is undetectable via conventional polarisation testing. The experiment reported herein highlights the (very) different behaviour between the two alloys with a similar Cu and Mg content (and similar bulk composition), especially in regards to the formation of a more stable passive film in the case of the AM2024. The formation of a more stable passive film was rationalised by the size and distribution of submicron sized particles, which are a direct result of the processing via SLM. The OCP corrosion rate analysis indicated that Cu/Al dissolution ratio was about one order of magnitude higher for the AM2024 compared to AA2024-T3. This refinement of microstructural features permits: i) more homogeneous dissolution of Cu-rich particles (Cu nano-particulates mechanically detaching from the surface as a consequence of Al dissolution), and ii) a significant decrease of the local cathode to anode surface area

ratio as compared to the wrought AA2024-T3 alloy. In such circumstances, the presence of a more stable oxide film under anodic polarisation would be plausible and rationalised by ICP-MS observations.

CONCLUSIONS

Herein, the microstructure and corrosion properties of AM prepared aluminium alloy 2024 (Al-3.6Cu-1.2Mg) were investigated. It was revealed that AM via the selective laser melting (SLM) process allowed for the development of a unique and refined microstructure, arising from the rapid solidification in the SLM process. The AM2024 microstructure obtained was unique in comparisons to wrought AA2024 as demonstrated by the preferential formation θ phase (over S-phase) and the absence of micron-sized particles. From the study reported herein, the following conclusions may be drawn:

- Observations using TEM and EDXS analysis revealed the absence of S-phase (Al₂CuMg), within the AM2024 alloy, which is in contrast to the prevalence of a high number density of S-phase precipitates in AA2024. The EDXS mapping supported the observed presence of high θ phase (Al₂Cu) number density, in addition to Mg₂Si and Al-Cu-Mn-Fe(-Si) phases. Furthermore, EDX mapping highlighted the presence of a heterogeneous distribution of the elements within the Al-Cu-Mn-Fe based particles, strongly suggesting a singular nucleation and segregation process.
- Electrochemical characterisation of AM2024 and wrought AA2024-T3 were performed in three different chloride containing electrolytes (0.01, 0.1, 0.6 M NaCl). Cathodic potentiodynamic polarisation testing in electrolytes of increasing chloride concentrations revealed minimal change in the cathodic current was noted. However, the pitting potential (of AM2024 was clearly distinguishable in 0.6 M NaCl and was around +90 mV vs. OCP. This finding suggests that the absence of S-phase, shifts the breakdown potential to more noble potentials, and retards corrosion.
- *In situ* monitoring of elemental corrosion rates in 0.01 M NaCl were determined for AM2024 and wrought AA2024-T3. Such *in situ* testing was carried out during both OCP exposure and during anodic polarisation testing. The dissolution profiles at OCP revealed a substantial difference in the corrosion behaviour between the two alloys; with the v_{Al} for AM2024 being ~5 times lower than the wrought AA2024-T3 at the end of the experiment duration. However, the quantity of alloying elements dissolved for the AM2024 was about one order of magnitude higher for Cu, Fe, and Mg. The dissolution of these alloying elements at the early stages of the corrosion is beneficial as it prevents the growth of potential cathodes that would induce further localised corrosion – however more generally points to a complex dissolution profile that is hitherto unreported – and merits important work in the future understanding of AM prepared Al-alloy dissolution.
- In addition to the free corrosion rates measured at OCP, the AESEC dissolution profiles during anodic polarisation also demonstrated the enhanced corrosion performance (i.e. a lower dissolution rate) of the AM2024 in comparison to wrought AA2024-T3. The difference between the i_c and i_{Al} signals measured revealed that the AM2024 was able to form a significantly thicker and more protective oxide film upon its surface. The dissolution characteristics measured here are an indicator of the improved corrosion resistance of AM2024. An enhanced corrosion performance may also be positively influenced by the absence of constituent particles in AM2024.

REFERENCES

- Birbilis, N., & Buchheit, R. G. (2005). Electrochemical characteristics of intermetallic phases in aluminum alloys: An Experimental survey and discussion. *Journal of The Electrochemical Society*, 152(4), B140–B151. <https://doi.org/10.1149/1.1869984>
- Birbilis, N., Cavanaugh, M. K., & Buchheit, R. G. (2006). Electrochemical behavior and localized corrosion associated with Al₇Cu₂Fe particles in aluminum alloy 7075-T651. *Corrosion Science*, 48(12), 4202–4215.
- Birbilis, N., Zhu, Y. M., Kairy, S. K., Glenn, M. A., Nie, J. F., Morton, A. J., ... Hughes, A. E. (2016). A closer look at constituent induced localised corrosion in Al-Cu-Mg alloys. *Corrosion Science*, 113, 160–171. <https://doi.org/10.1016/j.corsci.2016.10.018>

- Boag, A., Hughes, A. E., Wilson, N. C., Torpy, A., MacRae, C. M., Glenn, A. M., & Muster, T. H. (2009). How complex is the microstructure of AA2024-T3? *Corrosion Science*, 51(8), 1565–1568. <https://doi.org/10.1016/j.corsci.2009.05.001>
- Buchheit, R. G. (1997). Local dissolution phenomena associated with S Phase (Al_2CuMg) particles in aluminum alloy 2024-T3. *Journal of The Electrochemical Society*, 144(8), 2621–2628.
- Buchheit, R. G., & Birbilis, N. (2010). Electrochemical microscopy: An approach for understanding localized corrosion in microstructurally complex metallic alloys. *Electrochimica Acta*, 55(27), 7853–7859. <https://doi.org/10.1016/j.electacta.2010.04.046>
- Buchheit, R. G., Grant, R. P., Hlava, P. F., McKenzie, B., & Zender, G. L. (n.d.). *Local Dissolution Phenomena Associated With S Phase (Al_2CuMg) Particles in Aluminum Alloy 2024-T3*. Albuquerque, New Mexico.
- Caiazza, F., Alfieri, V., Argenio, P., & Sergi, V. (2017). Additive manufacturing by means of laser-aided directed metal deposition of 2024 aluminium powder: Investigation and optimization. *Advances in Mechanical Engineering*, 9(8), 1–12. <https://doi.org/10.1177/1687814017714982>
- Gharbi, O., Birbilis, N., & Ogle, K. (2016). In-situ monitoring of alloy dissolution and residual film formation during the pretreatment of Al-Alloy AA2024-T3. *Journal of The Electrochemical Society*, 163(5), C240–C251. <https://doi.org/10.1149/2.1121605jes>
- Gharbi, O., Birbilis, N., & Ogle, K. (2017). Li reactivity during the surface pretreatment of Al-Li alloy AA2050-T3. *Electrochimica Acta*, 243. <https://doi.org/10.1016/j.electacta.2017.05.038>
- Hou, L., Raveggi, M., Chen, X.-B., Xu, W., Laws, K. J., Wei, Y., ... Birbilis, N. (2016). Investigating the Passivity and Dissolution of a Corrosion Resistant Mg-33at.%Li Alloy in Aqueous Chloride Using Online ICP-MS. *Journal of The Electrochemical Society*, 163(6), C324–C329. <https://doi.org/10.1149/2.0871606jes>
- Lacroix, L., Blanc, C., Pébère, N., Thompson, G. E., Tribollet, B., & Vivier, V. (2012). Simulating the galvanic coupling between S- Al_2CuMg phase particles and the matrix of 2024 aerospace aluminium alloy. *Corrosion Science*, 64, 213–221. <https://doi.org/10.1016/j.corsci.2012.07.020>
- Lacroix, L., Ressler, L., Blanc, C., & Mankowski, G. (2008). Combination of AFM, SKPFM, and SIMS to Study the Corrosion Behavior of S-phase particles in AA2024-T351. *Journal of The Electrochemical Society*, 155(4), C131. <https://doi.org/10.1149/1.2833315>
- Leblanc, P., & Frankel, G. S. (2002). A Study of corrosion and pitting initiation of AA2024-T3 using atomic force microscopy. *Journal of The Electrochemical Society*, 149(6), 239–247. <https://doi.org/10.1149/1.1471546>
- Lebouil, S., Tardelli, J., Rocca, E., Volovitch, P., & Ogle, K. (2014). Dealloying of Al_2Cu , $\text{Al}_7\text{Cu}_2\text{Fe}$, and Al_2CuMg intermetallic phases to form nanoparticulate copper films. *Materials and Corrosion*, 65(4), 416–424. <https://doi.org/10.1002/maco.201307550>
- Martin, J. H., Yahata, B. D., Hundley, J. M., Mayer, J. A., Schaedler, T. A., & Pollock, T. M. (2017). 3D printing of high-strength aluminium alloys. *Nature*, 549(7672), 365–369. <https://doi.org/10.1038/nature23894>
- Mokaddem, M., Volovitch, P., Rechou, F., Oltra, R., & Ogle, K. (2010). The anodic and cathodic dissolution of Al and Al–Cu–Mg alloy. *Electrochimica Acta*, 55(11), 3779–3786. <https://doi.org/10.1016/j.electacta.2010.01.079>

- Nisancioglu, K. (1990). Electrochemical behavior of aluminum-base intermetallics containing iron. *Journal of The Electrochemical Society*, 137(1), 69–77.
- Ogle, K. (2012). Atomic emission spectroelectrochemistry: A new look at the corrosion, dissolution and passivation of complex materials. *Corrosion and Materials*, 37(3), 58–65.
- Polmear, I. J. (1995). *Light Alloys : Metallurgy of the light metals* (Third).
- Scamans, G. M., Birbilis, N., & Buchheit, R. G. (2010). Corrosion of Aluminum and its Alloys. In Tony Richardson (Ed.), *Shreir's Corrosion* (pp. 1975–2008).
- Scholes, F. H., Furman, S. A., Hughes, A. E., & Markley, T. A. (2006). Corrosion in artificial defects. I: Development of corrosion. *Corrosion Science*, 48(7), 1812–1826. <https://doi.org/10.1016/j.corsci.2005.05.050>
- Scully, J. R., Knight, T. O., Buchheit, R. G., & Peebles, D. E. (1993). Electrochemical characteristics of the Al₂Cu, Al₃Ta and Al₃Zr intermetallic phases and their relevancy to the localized corrosion of Al alloys. *Corrosion Science*, 35(1–4), 185–195.
- Serdechnova, M., Volovitch, P., Brisset, F., & Ogle, K. (2013). On the cathodic dissolution of Al and Al alloys. *Electrochimica Acta*. <https://doi.org/10.1016/j.electacta.2013.09.145>
- Zhang, H., Zhu, H., Qi, T., Hu, Z., & Zeng, X. (2016). Selective laser melting of high strength Al-Cu-Mg alloys: Processing, microstructure and mechanical properties. *Materials Science and Engineering A*, 656, 47–54. <https://doi.org/10.1016/j.msea.2015.12.101>
- Zhang, W., & Frankel, G. S. (2002). Localized Corrosion Growth Kinetics in AA2024 Alloys, 510–519. <https://doi.org/10.1149/1.1513984>